Effects of dimensions and regularity on the mechanical properties of the smectic phase formed during orientation-induced crystallization of poly(ethylene terephthalate)

Ren Tomisawa[a], Shun Oneda[a], Toshifumi Ikaga[a], KyoungHou Kim[a], Yutaka Ohkoshi[a,b*], Kazuyuki Okada[c],

Hiroyasu Masunaga[d], Toshiji Kanaya[e], Hiroo Katsuta[f], and Yoshitsugu Funatsu[f]

[a]*Faculty of Textile Science and Technology, Shinshu University, 3-15-1 Tokida, Ueda, Nagano 386-8567, Japan.*
E-mail: yokoshi@shinshu-u.ac.jp

[b]*Institute for Fiber Engineering, Shinshu University 3-15-1 Tokida, Ueda, Nagano 386-8567, Japan.*

[c]*Material Science Laboratories, Toray Research Center, Inc., 3-3-7 Sonoyama, Otsu, Shiga 520-8567, Japan.*

[d]*Japan Synchrotron Radiation Research Institute, 1-1-1 Kouto, Sayo-cho, Sayo-gun, Hyogo 679-5148, Japan.*

[e]*High Energy Accelerator Research Organization, 203-1 Shirakata, Tokai-mura, Naka-gun, Ibaraki, 319-1106, Japan.*

[f]*Fibers and Textiles Research Laboratories, Toray, 4845 Mishima, Shizuoka 411-8652, Japan.*

First Author: Ren Tomisawa, +819096696619 16st106j@shinshu-u.ac.jp

Corresponding Author; Yutaka Ohkoshi

Abstracts

A fibrillar-shaped metastable smectic phase forms during orientation-induced crystallization of poly(ethylene terephthalate). We investigated the effects of dimensions and regularity of the smectic phase on the mechanical properties by high-precision X-ray measurements. The drawing stress dependence was 76–168 MPa and the spinning speed dependence of 250–2000 m/min. The proportion, persistence length, and thickness of the smectic phase achieved their maximum values at 0.3–0.4 ms after necking. At this time g_{II} also reached a minimum value of 3.7%–4.3%. The persistence length increased linearly with the natural draw ratio of as-spun fibers at less than 1500 m/min. The maximum values of the proportion, persistence length, and thickness showed no dependence on the drawing stress; however, the proportion and persistence length increased more rapidly. The increase of d-spacing with drawing stress led to an apparent elastic modulus of approximately 40 GPa for the oriented molecular bundle.

Keyword: Smectic phase, Poly(ethylene terephthalate), Microfibril length, X-ray diffraction, Mechanical property

1. Introduction

Poly(ethylene terephthalate), commonly referred to as PET, is a semi-crystalline polymer widely used as a synthetic fiber owing to its excellent thermomechanical properties. The tensile strength and Young's modulus of PET fibers are improved by orientation-induced crystallization, which occurs during spinning and drawing processes. However, the properties of resultant fibers are difficult to estimate quantitatively from the microscopic structure. For example, the tensile strength of fibers rarely exceeds 5% of the theoretical value as estimated for complete PET crystals [1]. This result can be explained by the residual amorphous phase and uniformity of higher order structures. In particular the fibrillar structure, so-called fibrils or microfibrils are important, that is, the number and tautness of inter-fibril and intra-fibril tie-chains is thought to decide the tensile strength of the resultant fibers.

Microfibrils consist of sequentially repeating crystal and amorphous phases, with a long period of approximately 10 nm, as a stress bearing structure in PET fibers [2]. Microfibrils are long fibrillar structures having a thickness of a few nanometers perpendicular to the fiber axis. In on-line measurements based on continuous laser-drawing processing of PET, fibrillar-shaped metastable structures, were observed less than 1 ms after necking and disappeared with the appearance of crystal diffraction peaks and a long-period pattern [3-5]. In these studies, it was presumed that this structure is a precursor for microfibrils. This structure is called a smectic phase, which is the mesophase first reported by Bonart [6], and has also been reported for poly(ethylene naphthalate) [7] and poly(butylene terephthalate) [8]. The smectic phase has been reported during batch drawing [9] and heat treatments of oriented amorphous PET [10]. Abou-Kandil et al. used computer simulations to determine the necessary conditions for the appearance of the molecular chain conformation leading to the distinctive (001′) diffraction of the smectic phase [11]. The d-spacings of 1.017–1.068 nm [3-5, 12-15] and the effects of melt-spinning and drawing conditions on the intensity and d-spacing [16, 17] of the (001′) diffraction peak have also been reported. These reports indicated that the diffraction intensity increases with the draw ratio at first and the d-spacing seemed to increase after saturation of the intensity. However, the change in d-spacing is too small to enable a discussion of the relationship between the fibril structure development and the mechanical properties of the obtained fibers.

In this study, we improved the measurement resolution to analyze the effects of the drawing stress on the d-spacing change in a high drawing stress region. A higher resolution has been achieved with the use of an undulator-equipped synchrotron X-ray source and the high-resolution SOPHIAS X-ray detector [18]. We averaged many images taken at each elapsed time in time-course measurements over a continuous laser-drawing line. In addition to the proportion and d-spacing, we also estimated the persistence length, thickness, and second disorder parameter of the fibrillar smectic phase to quantify the uniformity of the molecular chain alignment in the microfibril. We estimated the second disorder parameter from a Hosemann plot of the (001′), (003′), and (005′) diffraction results. Our

analysis of the spinning speed and draw ratio dependence on the development of these structural parameters based on high-precision data enables us to discuss the quantitative contributions of inter-fibrillar and intra-fibrillar tie-chains to the mechanical properties of the resultant fibers.

2. Experimental

2.1 Samples

The fibers used for drawing were prepared by melt-spinning of PET (IV = 1.32 dL/g) supplied by Toray Industries, Inc. The polymer was heated at 300 °C and extruded from a one-hole nozzle at a mass flow rate of 5.0 g/min, and taken-up at 250–2000 m/min. The nozzle diameter was 1.0 mm, and the length/diameter ratio was 3.

2.2 Drawing

Fibers were drawn continuously by the speed difference between the feed and take-up rollers under heating by CO_2 laser irradiation [4]. The fiber running speed after necking was fixed at 130 m/min, and the draw ratio was controlled by changing the fiber-feed speed. A random polarized laser beam with a wavelength of 10.6 µm and a 6-mm spot diameter was generated by a PIN-30R laser (Onizuka Glass Co., Ltd.) and irradiated on to the running fiber from three different directions. The laser power for each drawing condition was determined so as to minimize the fluctuations of the neck-drawing point. The drawing tension was measured by a tension meter (HS-1500S, Eiko Sokki Co., Ltd.) with a 1-N pickup installed between the neck-drawing point and the take-up roller. The drawing stress was calculated from the drawing tension and the diameter of the drawn fiber. The drawing conditions are listed in Table 2.

2.3 On-line measurements

X-ray diffraction patterns were measured by irradiating the X-ray beam onto the running fiber. This on-line measurement system has been described in a previous report [4]. X-ray images were acquired at time points after necking by changing the distance between the X-ray irradiation point and necking point. The distance was changed with the necking point by moving the laser irradiation position. The elapsed time after necking was calculated from the distance divided by the fiber running speed. In particular for elapsed times less than 1.2 ms, the distance was measured accurately from video images taken during the measurement. The video images were acquired from the direction coaxial to the X-ray beam with a video camera (Watec Co., Ltd. WAT-232S type) equipped with a telecentric lens (OPTART Co., Ltd. TV-2S) with 2× magnification. In addition to the average position of the necking point, we also determined its fluctuation width from 10 still images taken from video images. These data were used to determine the time resolution of the measurements.

The synchrotron X-ray beam of SPring-8 BL03XU (FSBL) was used in this study. An undulator

was equipped to obtain ultrahigh-intensity X-ray beams. The wavelength of the X-ray beam was 0.10 nm and the beam dimensions were 60 µm × 100 µm along the vertical and horizontal directions. An X-ray image of the smectic (001′) diffraction peak was acquired by irradiating X-rays perpendicular to the fiber axis (0–2θ arrangement). To obtain high-resolution images, the diffraction patterns were acquired with a direct-detection X-ray SOI-CMOS 2D detector, SOPHIAS (1.9 Mpixels, 30 µm square pixels, imaging area of 26.7×64.8 mm^2) [18]. This system has integrating-type pixels [19] and was operated at 20 frames/s. To verify the precision of the measurements, 10 images were taken and analyzed individually and then averaged. The camera length was 543 mm, and the exposure time was 6 s for each image.

In addition to the measurements in the above mentioned 0–2θ arrangement, measurements in the θ–2θ arrangement were performed to analyze the smectic (003′) and (005′) diffractions. For this purpose, the fiber axis was tilted 8.2° from the normal plane of the X-ray beam. The X-ray wavelengths were set to be 0.06 and 0.10 nm for the (003′) and (005′) diffractions peaks, respectively. A Pilatus detector of 1043×981 pixel (172 µm/pixel) was used for this measurement. The camera length and exposure time were 310 mm and 20 s, respectively.

The time resolution of the measurements was calculated from the fiber speed and the position resolution, which was calculated from the length of the necking point (0.08–0.53 mm), width of the X-ray beam (0.1 mm), and the above-mentioned fluctuation width (0.15–0.30 mm) of necking point. A time resolution of 0.1–0.3 ms was obtained for both the 0–2θ and θ–2θ arrangements.

2.4 Birefringence

Birefringence for each fiber was measured on a polarized microscope (BX51-33POC, Olympus Co., Ltd.) with a 546-nm monochromic filter. Tricresyl phosphate was used as the immersion oil. The average and standard deviation of the birefringence were calculated for 10 samples.

2.5 Thermomechanical tests

Thermal and mechanical properties of the drawn fibers were analyzed by tensile testing, thermomechanical analysis (TMA), and differential scanning calorimetry (DSC). The tensile testing was performed by an Autograph AGS-X, Shimadzu Co. Ltd. equipped with a 50-N load cell. The sample length and elongation rate were 40 mm and 100%/min, respectively. The average and standard deviation of the strength, elongation, and Young's modulus were calculated for every ten samples. The natural draw ratio (NDR) was defined as the draw ratio at which the tensile stress began to rise again with dissipation of the necking point. A thermomechanical analyzer (TMA/SS6100, SII Nanotechnology Inc.) was used to measure the thermal shrinkage factor and shrinkage stress at heating rates of 5 and 10 K/min, respectively. The sample length was 10 mm for both measurements. DSC was performed on a calorimeter (Thermoplus DSC8230, Rigaku Co. Ltd.)

at a heating rate of 10 K/min. Short cut fibers were used as samples for DSC measurements. The melting point and crystallinity were determined from the peak position and the heat of fusion of the DSC curve. The heat of fusion of a PET crystal (135 J/g [20]) was used for the calculations.

3. Result and discussion

3.1 Properties and structures of PET fiber

The structure and physical properties of the as-spun fiber are shown in Table 1. The birefringence of the as-spun fiber increased with spinning speed, and the crystallinity also increased at more than 1000 m/min. The structure and physical properties of the drawn fiber are listed in Table 2. As the drawing stress increased from 80 to 170 MPa, the crystallinity of the drawn fiber changed little, and the birefringence and Young's modulus increased no more than 10%, whereas the tensile strength increased more than 20%, and the thermal shrinkage stress increased more than 50%. It has been reported that for fibers spun under conditions similar to those of this work, the proportion of the smectic phase increases sharply between 29–103 MPa, and almost saturates over 103 MPa [16]. The proportion of smectic phase was also saturated in this study (section 3.4) as indicated by the crystallinity data above. Hence, we will discuss the reasons for the increase in tensile strength and thermal shrinkage stress after saturation of the smectic phase on the basis of our high-resolution d-spacing measurements and the sizes of the smectic phase.

Table 1 Structure and properties of as-spun fibers

Spinning speed / m min^{-1}	NDR	Birefringence	Cold-crystallization temperature/°C	Melting temperature / °C	Crystallinity / %	Tensile strength / MPa	Elongation / %	Young's modulus / GPa
250	3.5	0.001	139	253	6	143	558	2.0
500	3.0	0.004	135	253	6	162	477	2.0
1000	2.1	0.010	129	252	9	208	347	2.1
1500	1.8	0.020	124	253	13	274	249	2.1
2000	1.5	0.038	121	252	15	319	175	2.3

Table 2 Structure and properties of drawn fibers

Sample *	Spinning speed / m min^{-1}	Drawing stress / MPa	Draw ratio	Laser power / W	Necking length /mm	Resolution time /ms	Birefringence	Melting temperature / °C	Crystallinity / %	Tensile strength / MPa	Elongation / %	Young's modulus / GPa	Maximum shrinkage / %	Maximum shrinkage stress	
														Stress / MPa	Temperature / °C
250-H	250	165	5.5	25.4	0.08	0.11	0.201	256	35	1080	20	10.9	22.1	85	184
250-M	250	103	5.0	24.9	0.10	0.10	0.187	256	36	940	29	9.8	19.6	66	165
250-L	250	76	4.7	24.5	0.14	0.11	0.180	255	30	850	39	8.8	19.1	50	167
500-H	500	168	4.6	26.2	0.11	0.14	0.184	256	36	1010	26	10.6	12.0	84	183
500-M	500	99	4.2	25.0	0.13	0.11	0.176	256	35	880	33	10.4	11.5	68	172
500-L	500	81	4.0	23.8	0.12	0.11	0.168	255	33	810	38	10.0	10.5	55	179
1000-M	1000	96	3.1	24.7	0.14	0.11	0.166	256	36	820	33	10.8	7.3	58	172
1500-M	1500	93	2.5	24.4	0.29	0.16	0.161	256	36	790	33	10.1	6.6	65	165
2000-M	2000	110	2.1	25.0	0.53	0.29	0.157	256	42	830	31	11.1	6.1	66	182

* Sample name : [Spinning speed / m min^{-1} – Drawing stress (High ~165 MPa / Medium ~100 MPa / Low ~80 MPa)]

3.2 Drawing Phenomena

Necking lengths are shown in Table 2. Because of the constant mass flow rate of 5.0 g/min, the diameter of the as-spun fiber decreased with spinning speed. The necking length clearly increased with the spinning speed, but hardly changed with the drawing stress despite the increase of the diameter change. Okumura et al. also reported that the necking length is almost independent of the drawing stress [21]. Because the take-up speed was fixed at 130 m/min in this study, a longer necking width requires a longer time for necking deformation, which might be explained by the uniformity of the network structure as discussed in section 3.6.

The fiber temperature profile was estimated from the energy balance equation considering the laser irradiation energy, heat transfer from the fiber surface, work of the external force of plastic deformation, and the latent heat of crystallization [4]. The necking point was decided by image analysis of video-images and the heat transfer coefficient was estimated by the empirical formula proposed Kase and Matsuo [22]. The absorption coefficient 1.149×10^4 (m^{-1}) [23] was used for the absorption of the PET fiber by the CO_2 laser. The heat of fusion of the drawn fiber (Table 3) was used as the heat of crystallization. The crystallization rate and crystallization induction time are listed in Table 3. For spinning speeds greater than 500 m/min, the reported values [16, 17] for the same spinning and drawing conditions are used for the calculation, whereas for 250 m/min, the values estimated from previous reports are used. The estimated fiber temperatures are also shown in Table 3. The temperature just before necking had little dependence on the drawing stress; however, the temperature immediately after necking increased with the drawing stress. The temperatures at the same drawing stress increased with spinning speed. The fiber temperature increased by 5–6 K within 0.3 ms from necking, at which point the smectic phase was most clearly observed by X-ray diffraction. The temperature at 0.3 ms represents a 35-K increase with the drawing stress and a 34-K decrease with the spinning speed.

Table 3 Fiber temperatures estimated for the drawing conditions

Sample	Heat of fusion / Jg^{-1}	Crystallization induction time / ms	Crystallization rate / 10^3 s^{-1}	Temperature immediately before the necking / $^\circ$C	Temperature immediately after the necking / $^\circ$C	Temperature at 0.3 ms after the necking / $^\circ$C	Max. Temp. / $^\circ$C & (Elapsed time / ms)
250-H	48			105	175	180	214 (2.2)
250-M	49	0.6 *	2.3 *	109	151	156	191 (2.2)
250-L	41			110	140	145	176 (2.2)
500-H	48	0.5 [17]	2.5 [17]	104	172	178	215 (1.9)
500-M	47	0.6 [17]	2.3 [17]	106	145	151	186 (2.1)
500-L	44	0.6 [17]	2.3 [17]	105	137	142	175 (2.2)
1000-M	49	0.5 [16]	3.7 [16]	97	131	138	176 (1.6)
1500-M	49	0.4 [16]	3.5 [16]	90	120	126	165 (1.5)
2000-M	57	0.4 [16]	7.7 [16]	84	117	122	167 (1.4)

* assumed value

3.3 X-ray diffraction images

X-ray diffraction images acquired for 500-M are shown Figure 1(a), and the meridional intensity profiles are shown in Figure 1(b). The streak-like diffraction shown at the right end of Figure 1(a) is the (001′) diffraction peak of the smectic phase. The (001′) diffraction peak appeared 0.1 ms after necking and achieved its maximum intensity at 0.3 ms, after which it gradually disappeared. The angle of the (001′) diffraction peak clearly increased with elapsed time. The intensity of the diffraction decreased with spinning speed but did not depend on the drawing stress.

Inclined X-ray diffraction images taken in the θ–2θ arrangement are shown in Figure 2. At a fixed tilt angle the X-ray wavelength was changed to locate the (003′) and (005′) reciprocal lattice points on the Ewald sphere. For all samples, the amorphous halo was concentrated in the equatorial direction by necking and the equatorial crystal diffractions appeared in the halo at 0.6 ms after necking. Diffraction peaks of the (−105) and (−103) crystal planes also appeared at 0.4−0.6 ms. In addition, streak-like meridian (001′), (002′), (003′), and (005′) diffraction peaks appeared 0.2 ms after necking. These diffraction peaks weakened at 0.4−0.6 ms accompanied by the appearance of (−105) and (−103) diffraction peaks.

The widths of the (00l′) diffraction peaks along both the meridional and equatorial directions appeared to increase with the diffraction order l. The equatorial widths of the (00l′) diffraction peaks are related to the disorientation and/or disordering of the molecular chains of the smectic phase. The former of these factors expands the peak width along the azimuthal angle, whereas the latter causes expansion along the direction perpendicular to the meridian. Kim et al. [12] attributed the widths of the (001′) and (003′) diffraction peaks to the effects of the disorientation and thickness. However, the increase of the azimuthal width with the diffraction order described above cannot be explained by the effects of either disorientation or thickness. Hence, we attribute this peak width behavior mainly to disorder of the chain arrangement along the chain axis. To evaluate the degree of disorder, we estimated the apparent thickness from the width of the (001′) diffraction peak perpendicular to the meridian.

The d-spacing and the persistence length of the smectic phase were also evaluated from the peak position and the meridian width of the (001′) diffraction. In addition, a second disorder parameter was obtained from the meridian widths of (001′), (003′), and (005′) diffraction features. The peak position and widths were obtained by peak fitting along each direction. The Gaussian and Pearson VII (Equation 1) functions were used to fit the profiles along and perpendicular to the meridian, respectively, as:

$$I_{(\varphi)} = \frac{I_0}{\left\{1 + 4\left(\frac{\varphi}{\beta_p}\right)^2 \left(2^{\frac{1}{m}} - 1\right)\right\}^m} \qquad (1)$$

where I, β_p, and $m = 2.0$ are the intensity, width, and shape factor of profile perpendicular to the meridional direction, respectively. The parameter $\varphi = \tan^{-1}(x/C)$ is the angle from meridian, in which x and C are the distance from the meridian and the camera length. All the obtained profiles showed good agreement with the measured profiles.
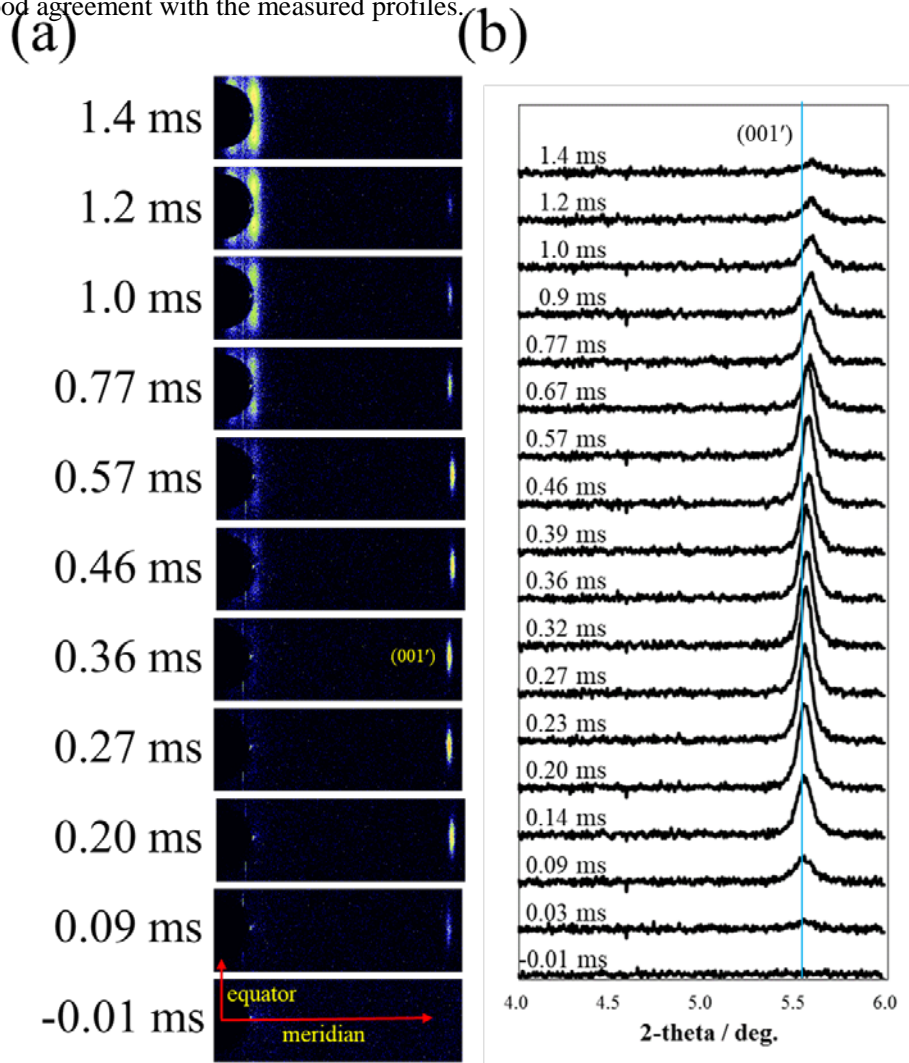

Figure 1 X-ray diffraction pattern (a) and meridional intensity profile (b) for 500-M. Times elapsed after necking are noted in the figure.
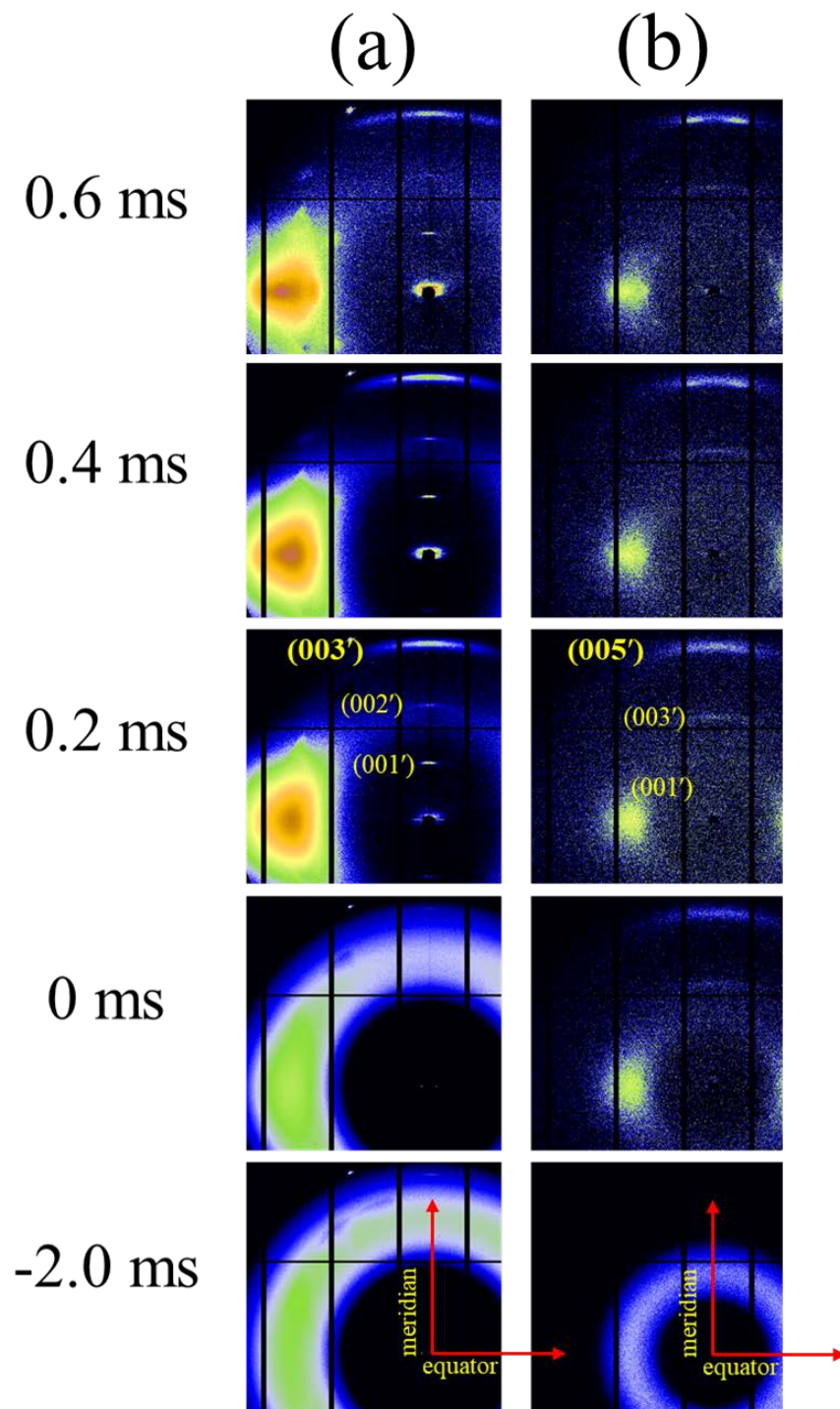
Figure 2 Inclined X-ray diffraction patterns for 500-M. Times elapsed after necking are noted in the figure. The fiber axis is inclined 8.2° from the meridian to fit the reciprocal lattice point of the (a) (003′) or (b) (005′) plane to the Ewald sphere by selecting the X-ray wavelength to be (a) 0.10 nm and (b) 0.060 nm.

3.4 Amount of smectic phase

The integrated intensities of the (001′) diffraction in the range of the diffraction angle 5°–6° are shown in Figure 3. Because the X-ray beam size in the direction perpendicular to the fiber of 60 μm was larger than the diameter of all the drawn fibers, we assumed that the X-ray beam irradiated the whole volume of the running fiber. Thus, the obtained integrated intensity was normalized by the X-ray irradiation volume. The intensity achieved a maximum at 0.3 ms after necking. The maximum intensity decreased with spinning speed but did not depend on the drawing stress. However, the intensity for drawing under the maximum drawing stress increased more rapidly than that at low drawing stress.
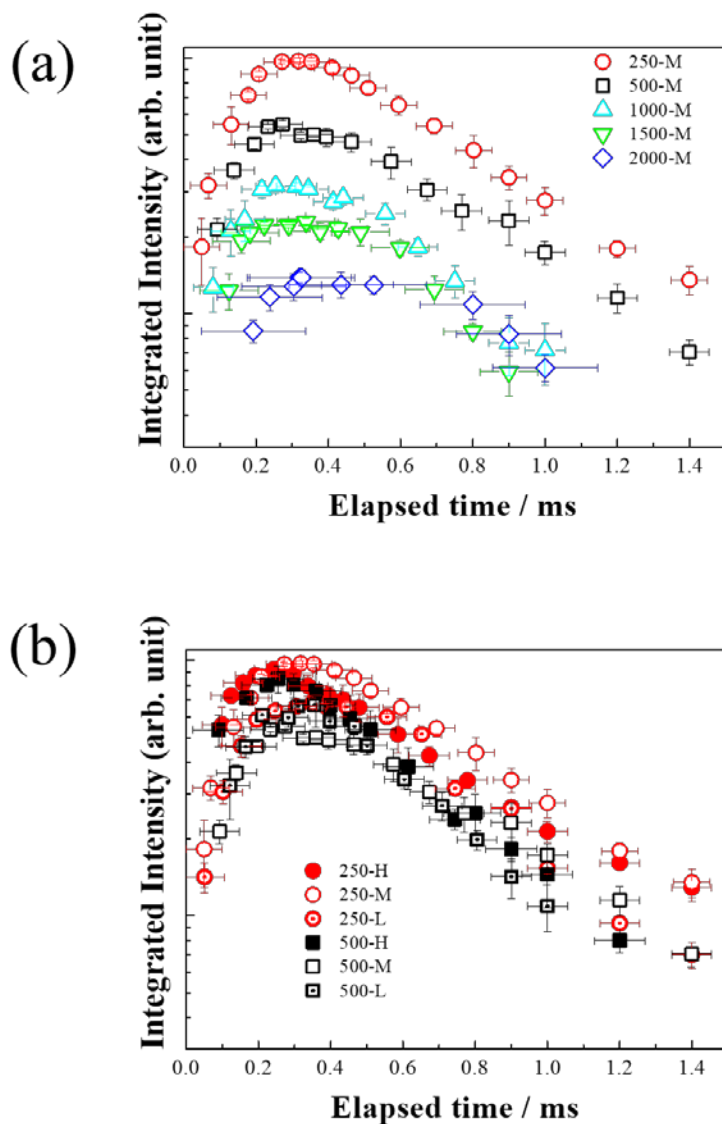
Figure 3 Integrated intensity of smectic (001′) diffraction peak normalized by the X-ray irradiated volume. Spinning speed dependence (a) and drawing stress dependence (b) are shown.

3.5 Size and disorder of microfibrils

The persistence length L and the apparent thickness D of the smectic phase were estimated by the Scherrer formula (2):

$$L = \frac{K\lambda}{\beta_a \cos\theta_a}, \qquad D = \frac{K\lambda}{\beta_p} \qquad\qquad (2)$$

where, λ is the X-ray wavelength and the constant K is 1. The half-diffraction angle θ_a, and integral widths (β_a, β_p) along and perpendicular to the meridian of the (001') diffraction were used for the calculation. The Hosemann's second disorder parameter g_{II} was calculated from Equation 3 [24]:

$$\left(\frac{\beta_m \cos\theta_m}{\lambda}\right)^2 = \left(\frac{1}{L}\right)^2 + \frac{(\pi g_{II} m)^4}{d^2} \qquad\qquad (3)$$

where β_m is the integral width of the (00m') diffraction peaks, and d is the d-spacing of the (001') diffraction. The integral widths β_3 and β_5 were obtained from the inclined measurements (Figure 2). The above-mentioned integral width of the (001') diffraction peak (β_a in Equation 2) for the corresponding elapsed time ±0.1 ms was used as β_1.

The calculated persistence length and thickness are shown in Figure 4 and 5, respectively. Both these factors showed a similar time dependence on the integral intensity, and both maximum values also showed a tendency to decrease with spinning speed and no dependence on the drawing stress. However, the persistence length increased rapidly at a higher drawing stress, and the thickness decreased rapidly after the maximum value at the maximum drawing stress. A typical Hosemann plot is shown in Figure 6. The points for the (001'), (003'), and (005') diffraction peaks were not aligned on a straight line for all elapsed times, all spinning speeds, and all drawing stresses. We obtained two sets of g_{II} values from the datasets of (β_1, β_3, β_5) and (β_1, β_3), which expressed almost the same features; however, the g_{II} values obtained from (β_1, β_3, β_5) showed greater deviation caused by the larger deviation of β_5 particularly at the longer elapsed time. The greater β_5 deviation for the longer elapsed time is likely caused by the effects of overlap with the (−105) diffraction peak. Therefore, we selected the g_{II} values obtained from (β_1, β_3) for Figure 7. Under all conditions, g_{II} reached a minimum value of 3.7%–4.3% at 0.4 ms after necking. The minimum g_{II} values were clearly greater than the g_{II} values reported for the c-axis direction of PET crystal (<1%) [25]. This result indicates a lower regularity of the molecular chain rearrangement along the chain axis in the smectic phase than that in the crystal.

In addition to the maximum of integrated intensity, the persistence length, thickness, and g_{II} also reached their minimum values 0.3–0.4 ms after necking. This elapsed time was almost the same as

the reported crystallization induction time of 0.3–0.5 ms [16, 17]. These results indicate that oriented molecular bundles of the nematic state formed by necking changes to the smectic phase up to 0.3–0.4 ms, followed by further changes to the crystals. The nematic–smectic transition requires an axial shift of the molecular chain in the oriented molecular bundle. Despite the long persistence length of 50–70 nm, which indicates well-aligned polymer chain bundles, the smectic phase shows a clearly larger g_{II} value than that of the crystal. Thus, we attribute the disorder of the molecular chain arrangement to an incomplete axial shift between the molecular chains. The tendency of the azimuthal width to increase with diffraction order (as shown in section 3.3) can also be explained by residual disorder between the molecular chains. The faster increase in the integral intensity and persistence length and the faster decrease in thickness observed for the higher drawing stress are also caused by the axial shift promotion of drawing stress. That is to say, the external force applied through the inter-fibrillar tie-chains promoted the axial shift and accelerated the nematic–smectic transition. However, the higher drawing stress likely preserved a greater disorder between the molecular chains, which contributed to the thinner apparent fibril thickness.
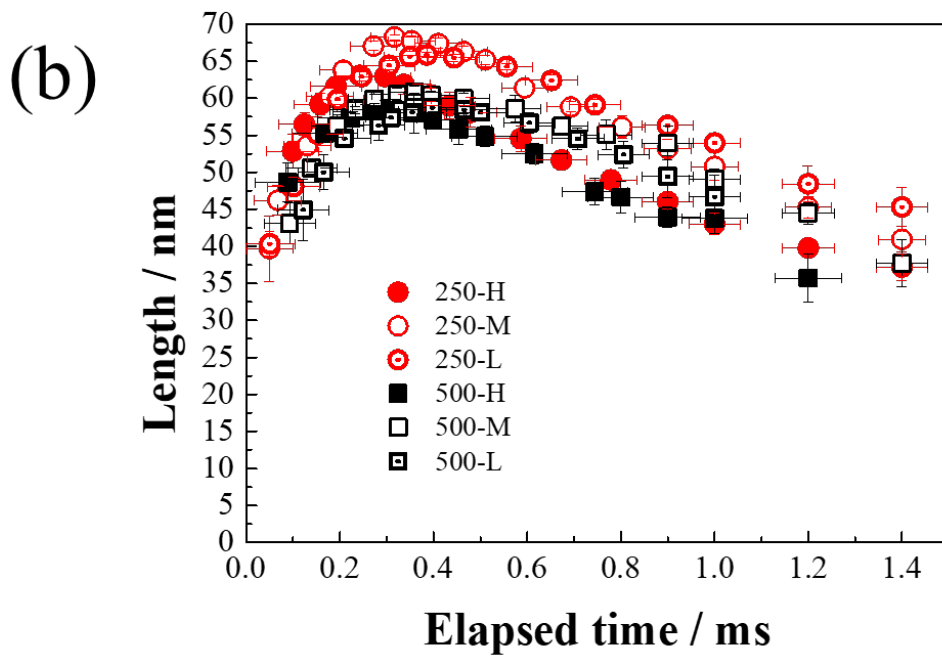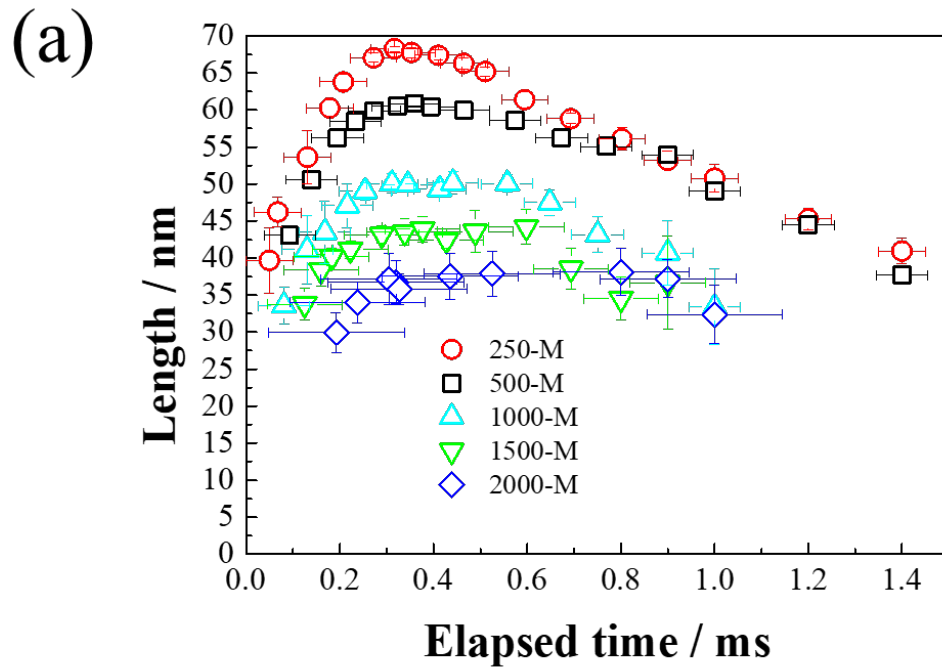
Figure 4 Persistence length of smectic phase estimated by equation 2. Spinning speed dependence (a) and drawing stress dependence (b) are shown.
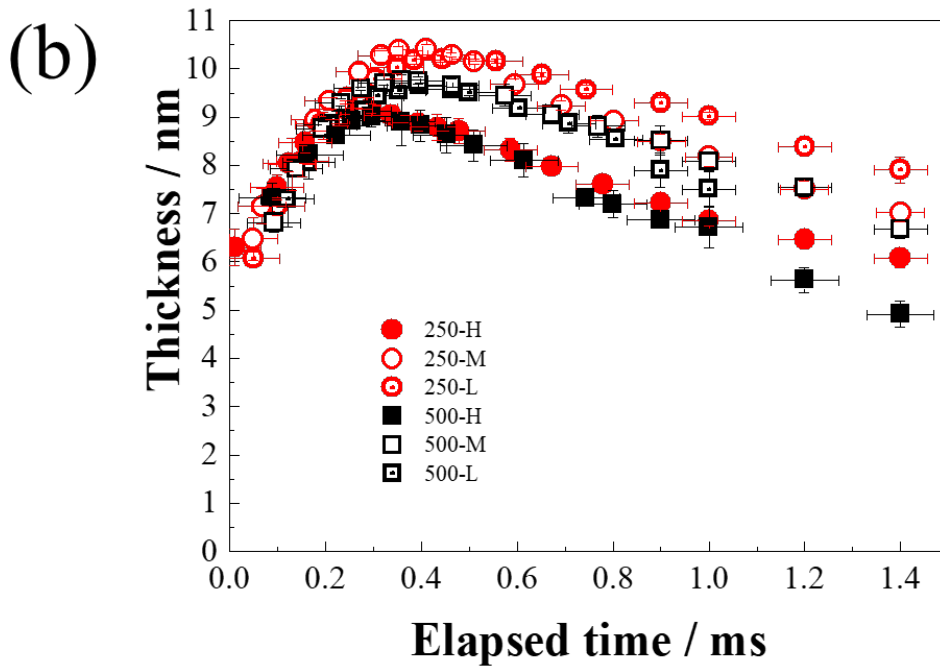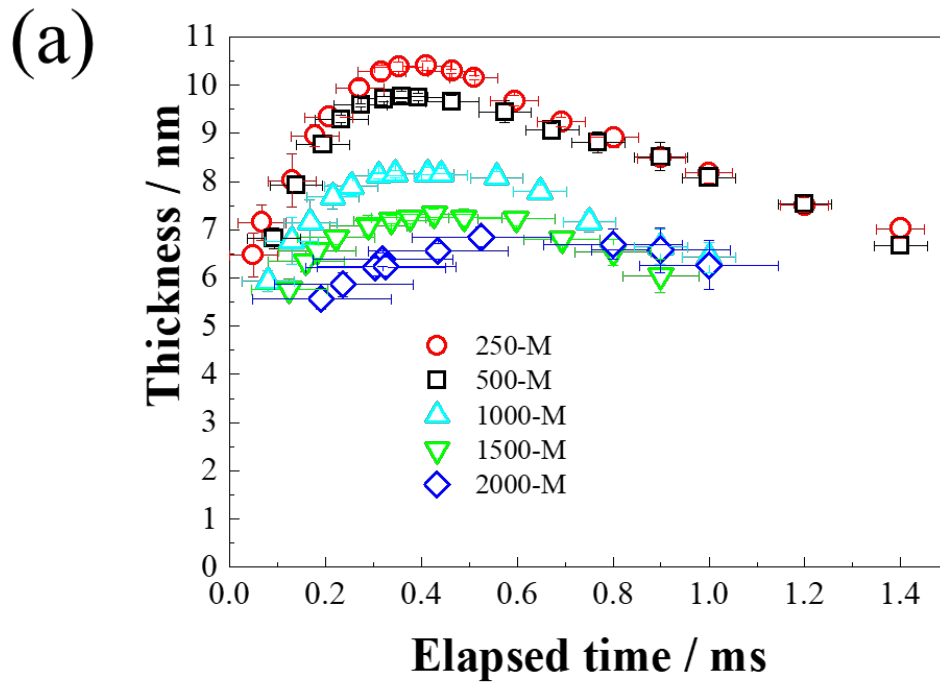
Figure 5 Thickness of smectic phase estimated by equation 2. Spinning speed dependence (a) and drawing stress dependence (b) are shown.
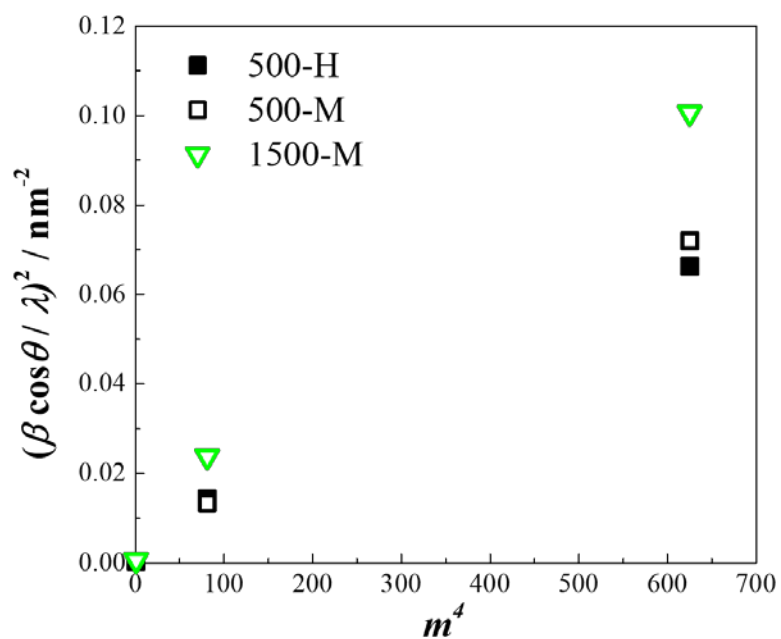
Figure 6 Hosemann plot for smectic (001′), (003′), and (005′) diffraction peaks at 0.4 ms. Sample names are noted in the figure.
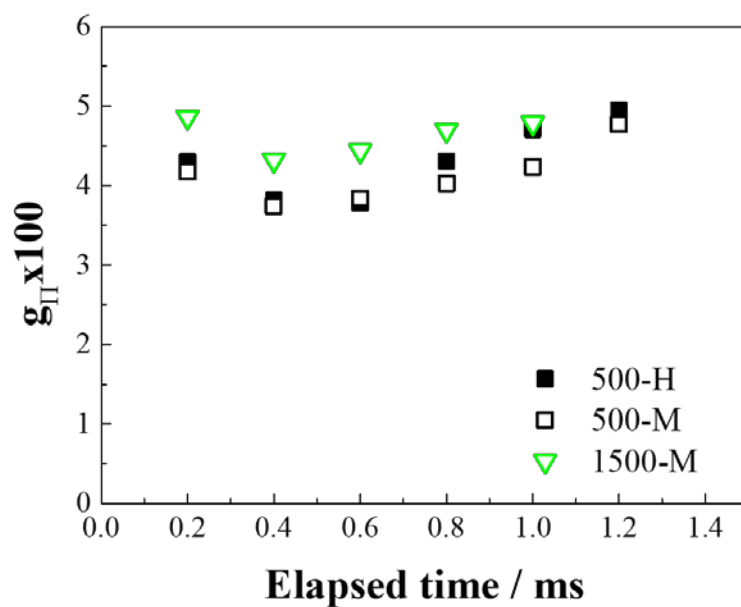

Figure 7 Disorder parameter g_{II} estimated from the smectic (001′) and (003′) diffractions following equation 3. Sample names are noted in the figure.

3.6 Uniformity in Network Structure

As shown in 3.5, the maximum persistence length strongly depends on the spinning speed but has little dependence on the drawing stress. The maximum persistence length plotted against the natural draw ratio (NDR) of the as-spun fiber is shown in Figure 8. The NDR, listed in Table 1, is considered to reflect the uniformity in the entanglement density and the chain orientation of the polymer chain network [1]. As shown in the figure, both the maximum persistence length and NDR decreased with spinning speed. In particular, at spinning speeds greater than 1500 m/min, the persistence length decreased more markedly.

As will be discussed in section 3.7, the smectic phase was considered to consist of well-aligned polymer chain bundles. Entanglements were excluded from the polymer chain bundle; thus, the maximum persistence length of the smectic phase was limited by the distance between entanglements. The decreases of both the maximum persistence length and NDR with spinning speed indicate that the spinning process determines the network structure, uniformity in the entanglement density, and chain orientation. Masubuchi et al. [26] reported that the uniformity in entanglement density decreased with spinning speed. That is, although the overall number of entanglements decreased with elongational deformation of the spinning the entanglement density near the chain ends hardly decreased. Owing to the decrease in the uniformity of entanglement density, the NDR decreased with the decrease in the shortest length of the network link bearing an external force. The decrease in the shortest length of the force-bearing network link should decrease the maximum persistence length of the smectic phase. The decrease in the uniformity should also increase the necking length, as shown in section 3.1, i.e., polymer networks with less uniformity require a longer time for yielding. The greater decrease in the persistence length than in the NDR observed at spinning speeds greater than 1500 m/min, as well as the clear decrease in the integral intensity and thickness, and the increase in g_{II}, can be explained by the stress concentration caused by oriented-nuclei formed in the spinning line [17]. Owing to stress concentration, the stress applied to the molecular bundle should decrease to suppress the axial shift of molecular chains.

The above results provide a structural basis for the empirical rule [1] that the maximum attainable strength of the PET fiber is determined mainly by the spinning conditions. As shown in Table 2, in this study fibers spun at higher speeds also had lower strength after drawing under the same drawing stress. The accessible drawing stress also generally decreases with spinning speed [17]. Therefore, the maximum attainable strength clearly decreases with spinning speed. The trend of the persistence length to decrease with spinning speed confirmed the validity of the obtained persistence length as a structural parameter for estimating uniformity in the entanglement density of polymer chain networks and the attainable maximum strength of resultant fibers.
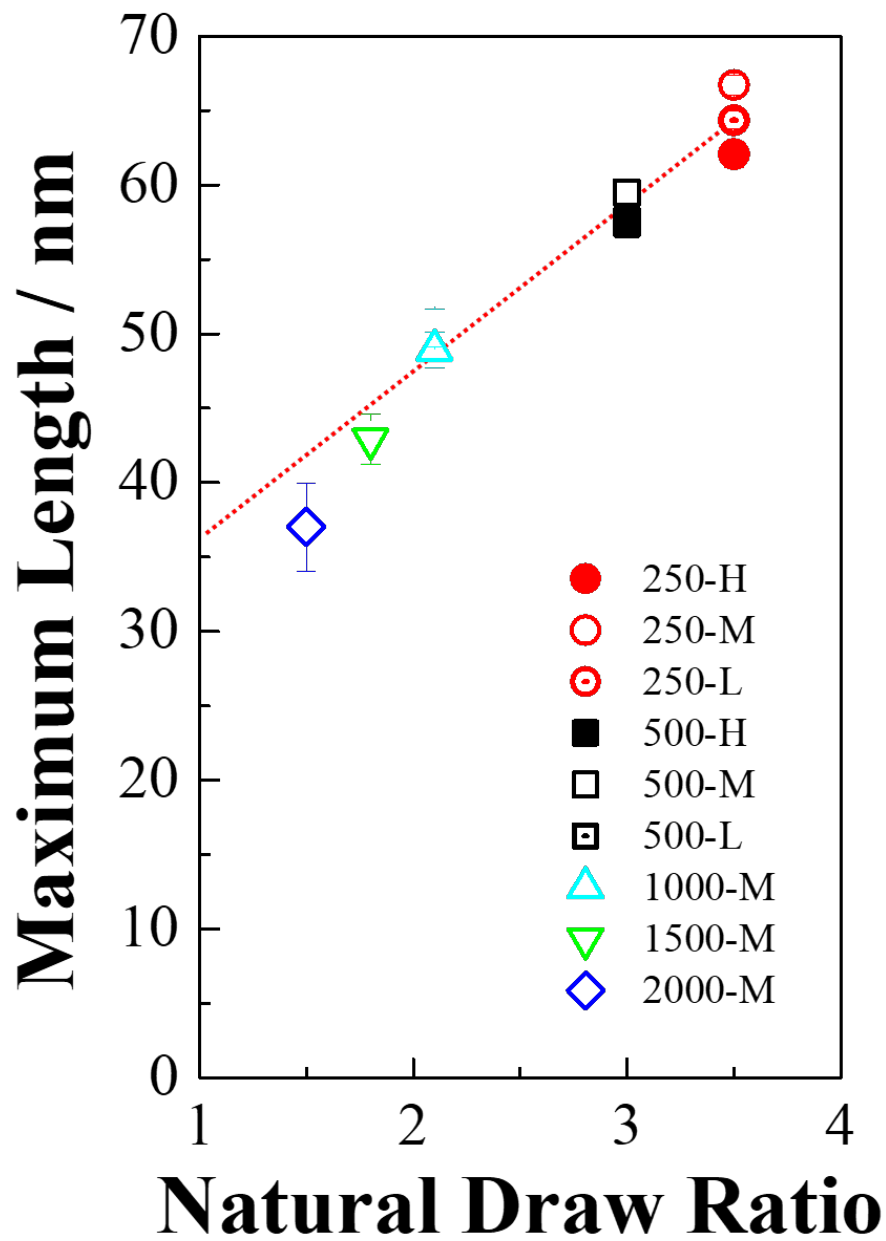
Figure 8 Observed maximum length of the smectic phase plotted against the NDR of the as-spun fiber. Sample names are noted in the figure.

3.7 d-spacing of smectic phase

The d-spacing d was determined by Bragg's equation (4):

$$2d\sin\theta = \lambda \qquad (4)$$

where θ is half of the (001′) diffraction angle. Obtained d-spacings are shown in Figure 9. All d-spacings decreased monotonically with time, and tended to decrease with spinning speed, in particular at spinning speeds of more than 1000 m/min. The larger variation at 2000 m/min is likely caused by the low intensity of the observed diffraction peaks.

Similar to the results of sections 3.4 and 3.5, the change in the d-spacing can be discussed separately before and after the elapsed time of 0.3–0.4 ms. Before that time, the change in d-spacing was strongly influenced by the spinning and drawing conditions, namely, a greater decrease was observed for fibers spun at higher spinning speeds or drawn under higher stress. The d-spacing continued to decrease after that time. The spinning-speed dependence of the d-spacing changed in the latter period, which corresponded well with the dependence of crystallization rate [17]. This result suggests that the d-spacing was decreased mainly by tilting of molecular chains owing to the phase transition from smectic to crystal [10, 16, 17]. Next, we consider the d-spacing in the earlier period, which is determined by the stress applied to the oriented chain bundle. In particular, the larger d-spacing observed in fibers formed under a higher drawing stress appeared to be caused by molecular chain extension. This presumption of molecular chain extension induced by the drawing stress is supported by the fiber temperature profiles measured by Yamaguchi et al. [27] and Kim et al. [5]. They reported that the measured fiber temperature immediately after necking was lower than the temperature estimated by assuming that the temperature increase was caused by work applied at the necking. The temperature difference increased together with the drawing stress, and disappeared with formation of the smectic phase. They suggested that a part of the applied work was stored as elastic energy, and released by relaxation of the extended molecular chain.

The d-spacing values of 1.017–1.068 nm [3-5, 12-15, 28] have been reported for the smectic phase formed in high-draw-ratio drawing of a low molecular orientation fiber. Previously reported d-spacings and those obtained in this study are plotted against the estimated fiber temperature (Figure 10). The d-spacings of approximately 0.3 ms were selected for the reported values, which had a time-resolution higher than 0.3 ms, whereas the maximum value was selected for the values having a lower time-resolution. All the d-spacings exceeded 95% for the crystal c-axis length of PET 1.077 nm [29], and tended to decrease with fiber temperature. The decreasing tendency can be explained by molecular chain shrinkage owing to entropic effects. The d-spacing value extrapolated to the room temperature was almost equal to the c-axis length of the crystal. Moreover, by using computer simulations, Abou-Kandil et al. revealed that all-trans conformations of methylene units

are required for the smectic (001′) diffraction peak to appear [11]. Therefore, the smectic phase can be regarded as a bundle consisting of perfectly oriented and almost fully extended molecular chains.
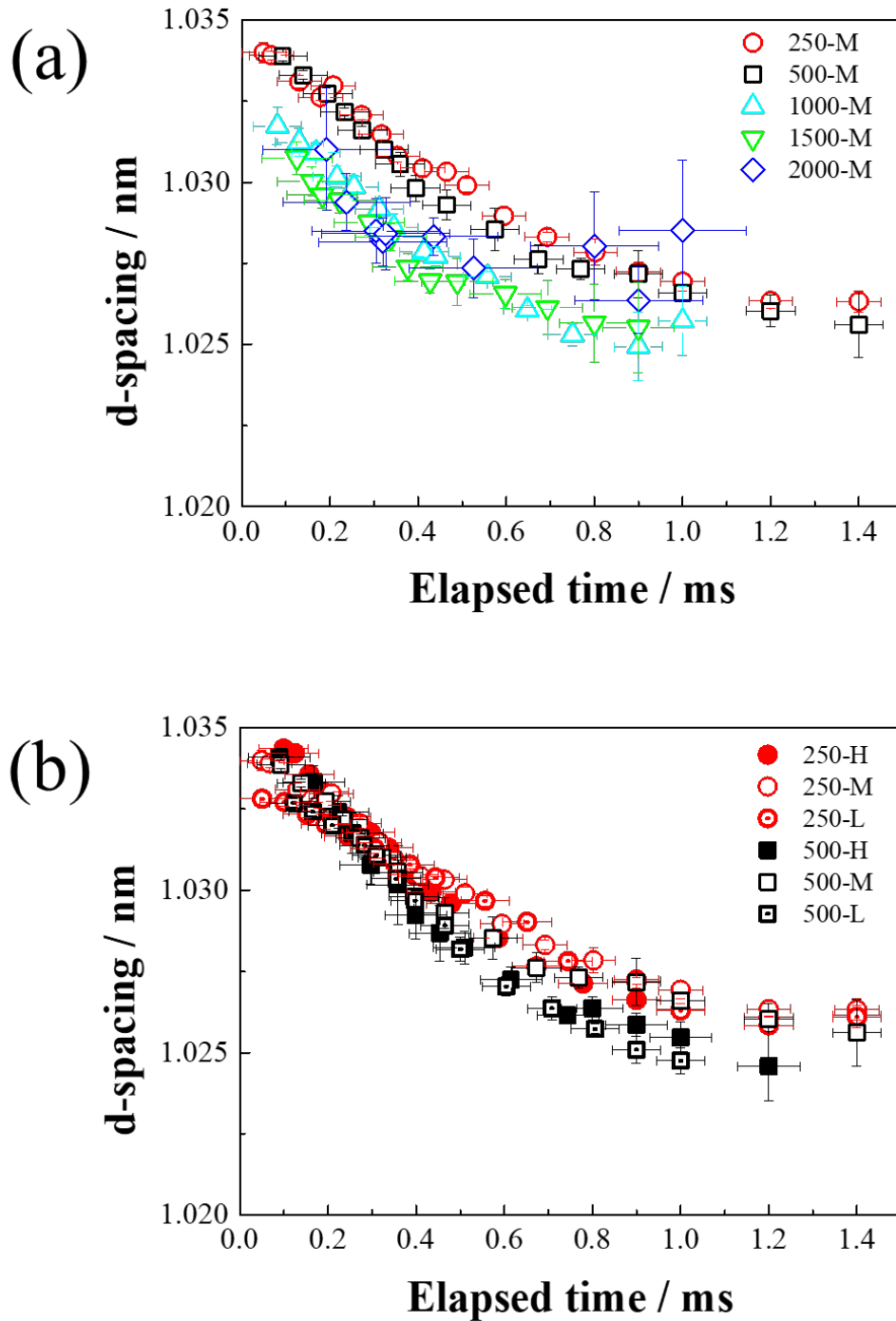

Figure 9 (a) Spinning speed and (b) drawing stress dependence on the d-spacing of smectic (001′) diffraction peak.
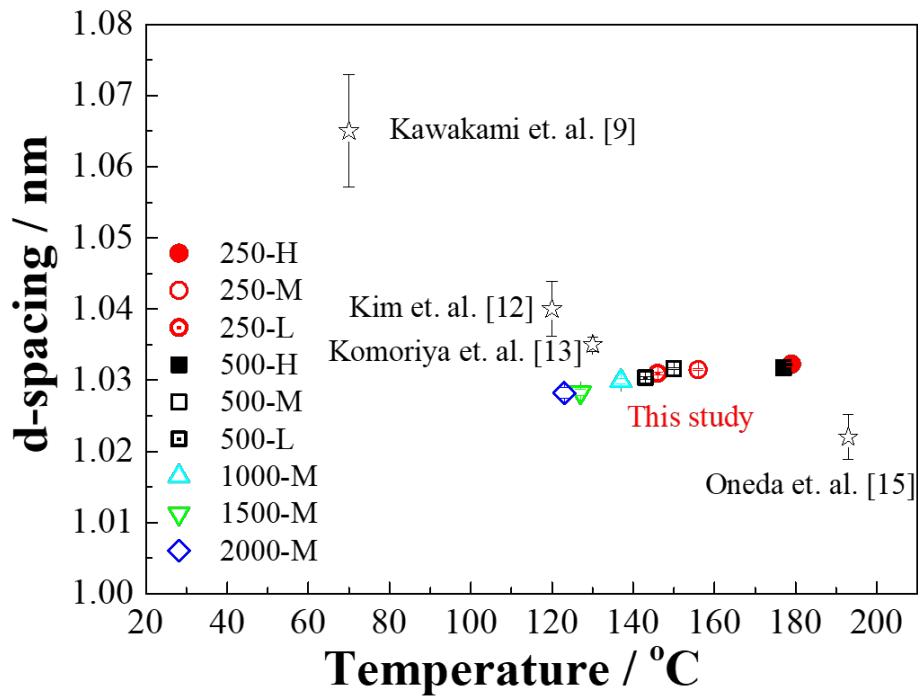
Figure 10 Reported d-spacing of smectic (001′) diffraction peak. Maxima or data for the maximum intensity around 0.3 ms, are plotted against the corresponding fiber temperature.

3.8 Modulus of the force-bearing molecular bundle

The high-resolution of the SOPHIAS detector enabled a nominal precision for the d-spacing of 0.6 pm. In fact, the standard deviations of all the obtained d-spacings shown in Figure 9 were less than 1 pm except for the data relating to very weak diffraction peaks. With the use of this high-precision d-spacing data, we tried to estimate the elastic modulus of the oriented molecular chain bundle from the drawing stress dependence. Figure 11(a) shows the same data as Figure 9; however, two data points of weak intensity, appearing immediately after necking at an elapsed time ~0.05 ms, were excluded because of their low accuracy. The d-spacing values measured from 0.10 to 0.25 ms indicated a clear drawing stress dependence but no clear spinning speed dependence between 250 and 500 m/min. The d-spacings lay on a straight line for each drawing stress within measurement error and appeared to converge at an elapsed time of 0.25–0.30 ms when the smectic formation was almost completed. This result suggests that the extended molecular chains relaxed with the axial shift between the chains. The average chain extension immediately after necking was estimated by extrapolating the d-spacing to the elapsed time zero. By plotting the extrapolated values against the drawing stress, as shown in Figure 11(b), the apparent elastic modulus of the oriented molecular

chain bundle was determined to be 40 GPa from the slope and intercept of the figure [30]. The accuracy of this value is not sufficiently high because the d-spacing depends on the fiber temperature, as shown above. That is, although the estimated fiber temperature for the same drawing stress increased no more than 6 K with elapsed time, the temperature increased up to 35 K with the drawing stress. A lower estimated modulus might be obtained by considering the temperature increase with drawing stress.

The obtained elastic modulus of 40 GPa is 1/3 smaller than the reported crystal modulus for PET (125 GPa), and 4 times as large as the Young's modulus of the drawn fibers (9–11 GPa). Because the fiber temperature immediately after necking was higher than the glass transition temperature of PET, only the orientated chain bundles, which account for approximately 1/3 of the molecules in the fiber cross-section, bear the drawing stress. Furthermore, when the obtained fibers were stretched at room temperature, the extension of microfibrils was considered to be limited to no more than 1/4 of the whole fiber extension because the modulus of microfibrils was no less than 40 GPa. As a result, most of the fiber strain can be attributed to the deformation of the inter-microfibrillar region.
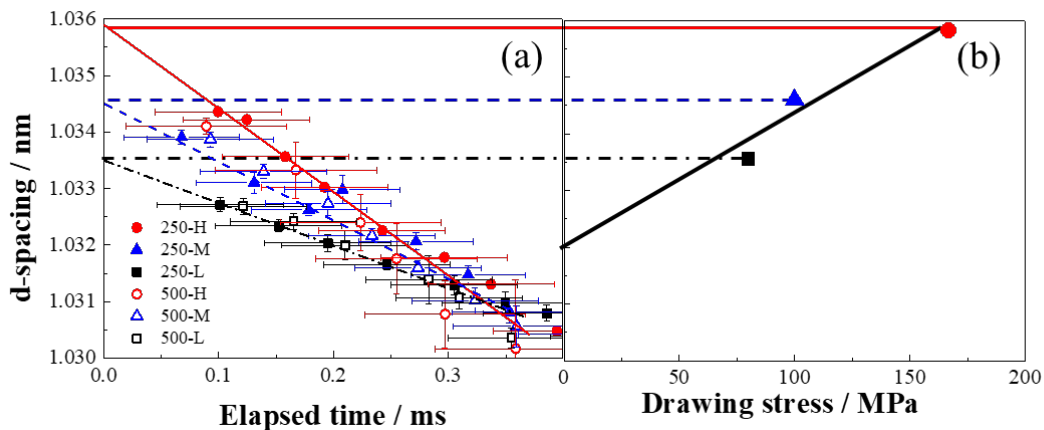

Figure 11 Extrapolation of (001′) d-spacings to the elapsed time of zero. An enlargement of Figure 9 (a) and extrapolated data are plotted against each drawing stress (b).

3.9 Model of the microfibril structure depends on the draw ratio

A schematic diagram of the drawing stress dependence on the fiber structure development is shown in Figure 12. This model is based on results for the minimum drawing stress [16] and the larger drawing stress obtained in this study. For the minimum draw ratio, which was almost the same as the NDR, no smectic phase was observed. The maximum persistence length and the proportion of smectic phase increased with drawing stress but effectively saturated over 80 MPa. Moreover, an X-shaped SAXS pattern was observed only for the minimum draw ratio [16], and the intensity of the layer-lined USAXS streak decreased with the draw ratio [31]. Hence, the crystallites that formed along the shear-band-like structure for the minimum drawing stress changed to a fibrillar smectic phase under a medium drawing stress. The arrangement of the fibrillar smectic phases along the shear-band-like structure became unclear at the maximum drawing stress.

As shown in Table 2, after saturation of the microfibril length and proportion, the Young's modulus and birefringence also saturated; however, the strength and thermal shrinkage stress of the drawn fiber continued to increase with drawing stress. The further increase in the strength and thermal shrinkage stress can be explained by the increase in the number and orientation of the inter-microfibrillar tie-chains connecting fibrils. The number and orientation of the inter-microfibrillar tie-chains should be lower than those of intra-microfibrillar tie-chains connecting crystallites in fibrils because inter-microfibrillar tie-chains consist of entanglement and molecular chain ends excluded from the oriented chain bundles whereas the intra-microfibrillar tie-chains should be formed by the fibrillar smectic phase.

Similar models that include a microfibril structure have already been proposed by Prevorsec [32] and Peterlin [2]. The originality of the current model is in the quantitative analysis of the fibrillar structure, in terms of the modulus, proportion, size, disordering, and arrangement. Through our analysis, the number and orientation of the inter-microfibrillar tie-chains can be discussed in greater detail. The relationship between the fibril structure formation and the uniformity of the network structure can also be discussed through the model. Hence, the mechanical and thermal properties of the fibers and films can be designed by choosing more appropriate processing conditions.
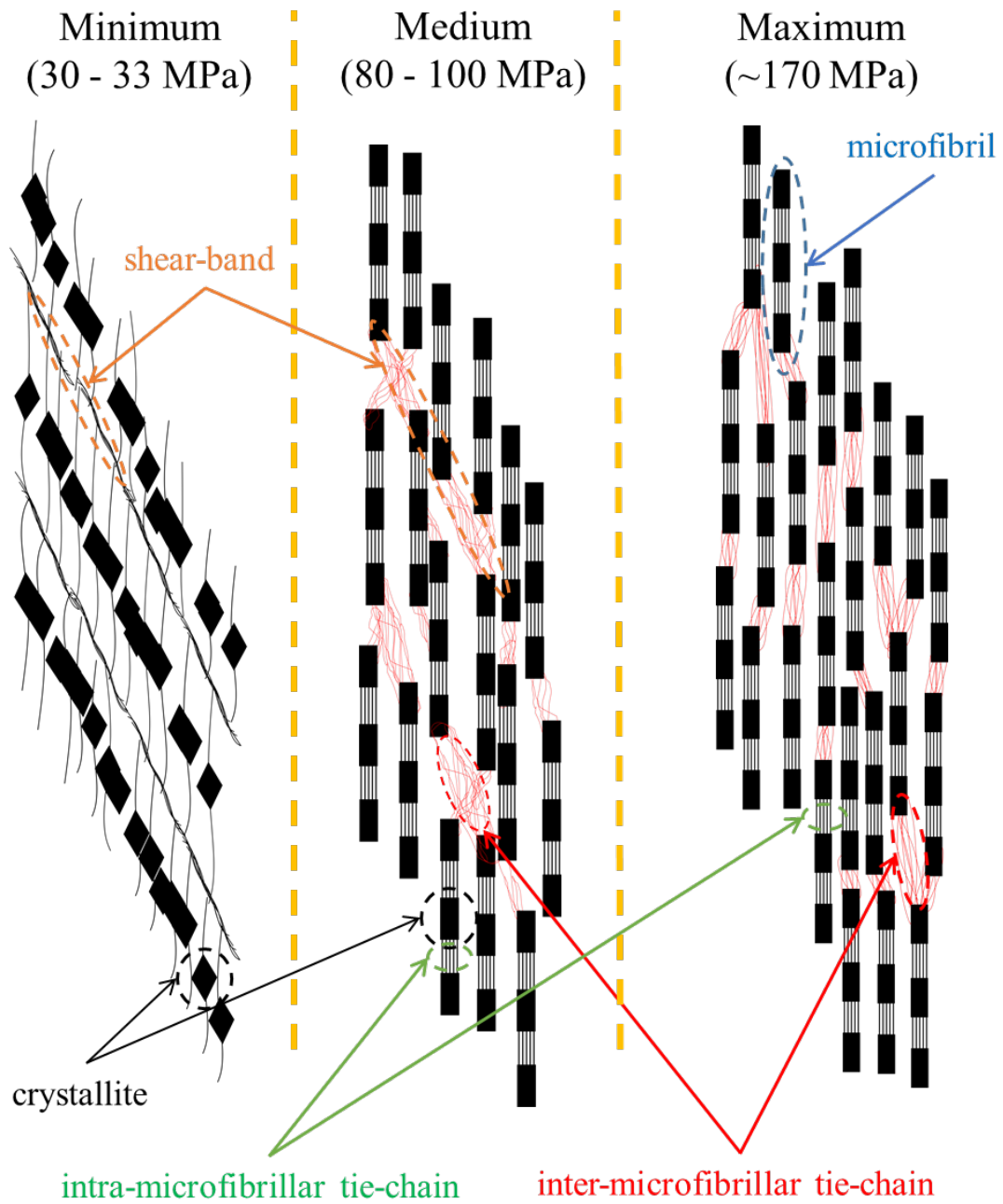
Figure 12 Schematic diagram of the drawing stress dependence on the fibril structure.

4. Conclusions

The effects of dimensions and regularity of a fibrillar-shaped smectic phase on mechanical properties of fibers were investigated by high-precision X-ray measurements with the use of the SOPHIAS detector. The drawing stress was set to be 76–168 MPa, a range over which the proportion of the smectic phase is reportedly almost saturated. The spinning speed dependence of 250–2000 m/min was also measured under a fixed drawing stress of approximately 100 MPa. Changes in the proportion, d-spacing, persistence length, and thickness of the smectic phase were measured from the intensity, peak position, and widths of the smectic $(001')$ diffraction peak, from just before necking to 1 ms after necking. Hosemann's g_{II} parameters were also determined from the meridian widths of the $(001')$ diffraction peak, and the $(003')$ and $(005')$ diffraction peaks obtained by inclined measurements.

The proportion, persistence length (50–70 nm) and thickness achieved maximum values, and g_{II} reached a minimum value (3.7–4.3%) at 0.3–0.4 ms after necking. The maximum and minimum values clearly depended on the spinning speed but showed little dependence on the drawing stress. The g_{II} value increased with spinning speed suggesting an incomplete axial shift between molecular chains. The persistence length and NDR of the as-spun fiber showed a linear relationship; however, a greater decrease in the persistence length than the NDR was observed at more than 1500 m/min.

The maximum value of the proportion and persistence length and thickness showed almost no dependence on the drawing stress. However, the proportion and persistence length increased more rapidly with drawing stress, and the thickness decreased more rapidly for the maximum drawing stress. The d-spacing of the smectic phase tended to decrease with temperature. Because the value extrapolated to room temperature almost corresponded to the crystal c-axis length, the smectic phase can be regarded as a bundle consisting of perfectly oriented and almost fully extended molecular chains. By increasing the d-spacing with drawing stress, an apparent elastic modulus of approximately 40 GPa was obtained for the oriented molecular bundle. This value suggests that external force concentrates on inter-microfibrillar tie-chains during tensile testing. We explain the considerable increase in tensile strength and thermal shrinkage stress, compared with the increase in the Young's modulus and birefringence, as drawing stress was increased, by the difference in the number and orientation of inter-microfibrillar tie-chains.

References

1) T. Kikutani et al. "*Fundamental and Practical Technologies for Nano-structured Polymeric Materials*", 2008, p.56-110, CMC press, ISBN978-4-7813-0043-6.

2) A. Peterlin, *J. Polym. Sci.*, A-2, 7, (1969), 1151.

3) T. Yamaguchi, K. Komoriyama, Y. Ohkoshi, H. Urakawa, Y. Gotoh, N. Terasawa, M. Nagura, K. Kajiwara, J. Polym. Sci., Polym. Phys., 43, (2005), 1090-1099.

4) T. Yamaguchi, K. H. Kim, T. Murata, M. Koide, S. Hitoosa, H. Urakawa, Y. Ohkoshi, Y. Gotoh, M. Nagura, M. Kotera, K. Kajiwara, J. Polym. Sci., Polym. Phys., 46, (2008), 2126-2142.

5) K. H. Kim, T. Yamaguchi, Y. Ohkoshi, Y. Gotoh, M. Nagura, H. Urakawa, M. Kotera, T. Kikutani, J. Polym. Sci., Polym. Phys, 47, (2009), 1653-1665.

6) R. Bonart, Kolloid-Z, 213, (1966), 1-11.

7) K. H. Kim, R. Aida, Y. A. Kang, T. Ikaga, Y. Ohkoshi, I. Wataoka, H. Urakawa, Polymer, 53, (2012), 4272-4279.

8) T. Konishi, Y. Miyamoto, Polymer, 42, (2010), 349-353.

9) D. Kawakami, B. S. Hsiao, C. Burger, S. Ran, C. Avila-Orta, I. Sics, T. Kikutani, B. Chu, Macromolecules, 38, (2005), 91-103.

10) T. Asano, F. J. Balta Calleja, A. Flores, M. Tanigaki, M. Mina, C. Sawatari, H. Itagaki, H. Takahashi, I. Hatta, Polymer, 40, (1999), 6475-6484.

11) A. I. Abou-Kandil, G. Goldbeck-Wood, A. H. Windle, Macromolecules 40, (2007), 6448-6453

12) K. H. Kim, T. Murata, Y. A. Kang, Y. Ohkoshi, Y. Gotoh, M. Nagura, H. Urakawa, Macromolecules, 44, (2011), 7378-7384.

13) A. Komoriya, R. Aida, K. H. Kim, Y. Ohkoshi, I. Wataoka, H. Urakawa, Fiber preprints, Japan, 56, (2010), 303.

14) K. Sugawara, T. Ikaga, K.H. Kim, Y. Ohkoshi, K. Okada, H. Masunaga, T. Kanaya, M. Masuda, Y. Maeda, Polymer, 79, (2015), 37-46.

15) S. Oneda, R. Tomisawa, T. Ikaga, K. H. Kim, Y, Ohkoshi, K. Okada, H. Masunaga, T. Kanaya, Y. Funatsu, M. Masuda, H. Katsuta, Fiber preprints, Japan, 72, (2017), 1B11.

16) R. Tomisawa, T. Ikaga, K.H. Kim, Y. Ohkoshi, K. Okada, H. Masunaga, T. Kanaya, M. Masuda, Y. Maeda, Polymer, 116, (2017), 367-377.

17) R. Tomisawa, T. Ikaga, K.H. Kim, Y. Ohkoshi, K. Okada, H. Masunaga, T. Kanaya, M. Masuda, Y. Maeda, Polymer, 116, (2017), 357-366.

18) T. Hatsui, M. Omodani, T. Kudo, K. Kobayashi, T. Imamura, T. Ohmoto, A. Iwata, S. Ono, Y. Kirihara, T. Kameshima, *Proc. Int. Image Sensor Workshop*, 2013, Art. No. 3.05. http://www.imagesensors.org/Past%20Workshops/2013%20Workshop/2013%20Papers/03-_05 8_hatsui_paper.pdf

19) T. Hatsui, H. Graafsma, *IUCrJ* 2015, 2, (3), 371-383.

20) A. Mehta, U. Gaur, B. Wunderlich, *J. Polym. Sci. Polym. Phys.* Ed. 16, (1978), 289.

21) W. Okumura, T. Kanegae, Y. Ohkoshi, Y. Gotoh, M. Nagura Polymer Processing XVIII, (2003), 1-7.

22) S.Kase, and T.Matsuo, Journal of Polymer Science Part A: General Papers, 3, (1965), 2541.

23) W. Okumura, T. Yamaguchi, Y. Ohkoshi, Y. Gotoh, M. Nagura, Intern. Polym. Proc., 17, (2002), 124-132.

24) R. Hosemann, S. N. Bagchi, "*Direct Analysis of Diffraction by Matter*" (North-Holland, Amsterdam, 1962) Ch. 9.

25) J. Shimizu, T. Kikutani, A. Takaku, N. Okui, *Sen'i Gakkaishi* 40, (1984), 177-183.

26) Y. Masubuchi. "Fundamental and Practical Technologies for Nano-structured Polymeric Materials", 2008, p.66-74, CMC press, ISBN978-4-7813-0043-6.

27) T.Yamaguchi, Y. Ohkoshi, Y. Gotoh, M. Nagura, *Seikei-Kakou* 17, (2005), 649-653.

28) K. Okada, K. Nakata, Y. Higashioji, K. Takahashi, Y. Ohkoshi, T. Kanaya, *Kobunshi Ronbunshu*, 71, 11, (2014), 593-600.

29) Y.Y. Tomashpol′skii, G.S. Markova, *Polym. Sci.* USSR 6, (1964), 316-324.

30) I. Sakurada, T. Itou, *Koubunnsi Kagaku*, 19, (1962), 300-305.

31) R. Tomisawa, T. Ando, T. Ikaga, K. H. Kim, Y. Ohkoshi, K. Okada, H. Masunaga, T. Kanaya, H. Katsuta and Y. Funatsu, *Polymer journal* submitted.

32) D. C. Prevorsec, *J. Polymer Sci. Symposium* no. 32 (1971).